Journal of Materials Chemistry A

ROYAL SOCIETY OF CHEMISTRY

PAPER

View Article Online
View Journal | View Issue

Check for updates

Cite this: J. Mater. Chem. A, 2025, 13, 38850

Stabilizing copper nanoparticles for electrochemical nitrate reduction *via* encapsulation inside carbon nanotubes

Tamilselvi Gurusamy, †[a] Thomas D. Pope, †[a] Samuel F. Wenzel, [a] He Zhang, [a] Heekwon Lee [a] and Hang Ren *[abc]

Received 1st July 2025
Accepted 13th October 2025

DOI: 10.1039/d5ta05291b

rsc.li/materials-a

Electrochemical nitrate reduction is an attractive pathway to synthesize ammonia from abundant nitrate sources. Copper (Cu) is an active catalyst for this transformation; however, its stability is often compromised by oxidation and leaching during electrocatalysis. Herein, we investigated the encapsulation of Cu nanoparticles inside carbon nanotubes (Cu-in-CNT), which significantly enhances both their structural and electrochemical stability compared to Cu nanoparticles supported on the outer surface (Cu-on-CNT). Encapsulation provides a protective environment that preserves the structure of the catalyst. Post-catalysis analysis reveals that Cu-in-CNT retains its metallic state, whereas Cu-on-CNT undergoes transformation to and CuO to Cu and Cu_2O. After 12 hours of continuous nitrate reduction, Cu-in-CNT exhibits much less Cu leaching (5.3 wt%) compared to Cu-on-CNT (20.5 wt%). Furthermore, Cu-in-CNT maintains a stable faradaic efficiency for nitrite and ammonia combined (~80%), in contrast to significant declined observed for Cu-on-CNT (~40%).

1 Introduction

Ammonia (NH_3) is a cornerstone chemical with key applications in agriculture, pharmaceuticals, and chemical manufacturing, and is increasingly recognized as a promising next-generation energy carrier. Currently, over 90% of global ammonia is produced *via* the Haber–Bosch process, which, despite its transformative impact on modern agriculture, operates under energy-intensive conditions (*i.e.*, $T = 400$–500 °C and $P = 150$–300 bar).[1–3] This process accounts for 1–2% of global energy consumption and ~1% of global CO_2 emissions.[4,5] Consequently, efforts have been diverted to developing a sustainable, room-temperature alternatives for ammonia synthesis. Although electrochemical nitrogen (N_2) reduction has attracted recent attention, its practical implementation remains challenging due to the difficulty in activating the highly stable N≡N triple bond and the low solubility of N_2 in aqueous solutions.[6–8]

Electrochemical nitrate reduction is an alternative pathway for ammonia synthesis.[9–12] Unlike N_2, nitrate (NO_3^-) and other NO_x intermediates can be activated under much milder conditions, and exhibit high solubility in aqueous solutions. Moreover, nitrate is abundantly available, including the widespread accumulation of reactive nitrogen compounds in the environment from agricultural runoff and fossil fuel combustion. Therefore, electrochemical reduction of nitrate to ammonia presents a sustainable and dual-benefit solution for (i) pollution mitigation through the removal of harmful nitrates from water, and (ii) the sustainable production of ammonia from an abundant waste stream.[13]

[a]Department of Chemistry, The University of Texas at Austin, Austin, TX 78712, USA. E-mail: hren@utexas.edu
[b]Texas Materials Institute, The University of Texas at Austin, Austin, TX 78712, USA
[c]Center for Electrochemistry, The University of Texas at Austin, Austin, TX 78712, USA
† Equal contribution.

Hang Ren

Hang Ren is an Assistant Professor at the University of Texas at Austin. He received B.S. in Chemistry from Sun Yat-Sen University (2011) and PhD Analytical Chemistry from the University of Michigan (2016) under Prof. Mark Meyerhoff, followed by postdoctoral training with Prof. Henry White at the University of Utah. Currently, his lab develops electroanalytical and imaging methods to uncover interfacial heterogeneity and dynamics in electrochemistry, advancing electrocatalysis, energy storage, and biology. Dr Ren's honors include NSF CAREER Award, DARPA Young Faculty Award, DARPA Director's Award, SEAC Young Investigator Award, Sloan Research Fellowship, NIH MIRA, Scialog Fellowship, and ACS Rising Star in Measurement Science.

Despite its promise, the practical application of electrochemical nitrate reduction is limited by sluggish kinetics arising from the multi-step proton–electron transfer processes, which generate undesired byproducts and compromise catalyst selectivity. Among various candidates, Cu-based catalysts have shown notable potential due to their favorable binding energies toward nitrate and key nitrogen intermediates, facilitating stepwise reduction to ammonia.[14–18] However, Cu catalysts, especially Cu nanoparticles, suffer from significant stability issues because they are prone to oxidation, aggregation, and structural degradation during extended operation. For example, electrodeposited Cu can quickly form surface oxides upon air and electrolyte exposure, which affect the selectivity and yield of ammonia even when they can be reduced back during nitrate reduction.[19–22] Furthermore, Cu^+ states, which are essential for stabilizing intermediates, are often over-reduced, thereby undermining catalyst integrity.[23,24] Metallic Cu nanoparticles are also susceptible to coalescence and dissolution, leading to active surface area loss and performance decay. Prior studies have shown that Cu nanoparticles, despite their high activity, are vulnerable to dynamic morphological changes that compromise long-term stability.[25–31]

To address these challenges, we hypothesize that confining Cu nanoparticles in a microenvironment can create a barrier that limits their aggregation and degradation during nitrate reduction, stabilizing the catalyst. Herein, we test this hypothesis by encapsulating Cu nanoparticles inside carbon nanotubes (CNTs). Encapsulation provides a physical barrier that limits particle–particle contact, which is necessary for aggregation. The isolation of Cu nanoparticles between different CNTs also impedes Ostwald ripening, which is another pathway for the degradation of nanoparticle catalyst. By comparing the catalyst morphology and selectivity of electrochemical nitrate reduction for Cu nanoparticles on CNTs *vs.* encapsulated inside the CNTs, the effectiveness of the strategy is directly demonstrated.

2 Materials and experimental methods

2.1 Materials

Multi-walled carbon nanotubes (dia: 20–40 nm, length: 1–2 μm, 95% purity) were purchased from TCI. Copper nitrate trihydrate (99%) was obtained from Acros Organics. Hydrochloric acid (36.5–38.0%), sodium hypochlorite solution (5.6–6%), sodium hydroxide (≥97%), and *o*-phosphoric acid (85%) were obtained from Fisher Scientific. Potassium nitrate (99%) was obtained from Alfa Aesar. Sodium dihydrogen phosphate (≥99.0%) and disodium hydrogen phosphate (≥99.0%) were obtained from Sigma-Aldrich. Nitric acid (70%), sodium nitrite (99.999%), sodium nitroferricyanide dihydrate (>99%), sodium salicylate (99%), and *N*-(1-naphthyl)-ethylenediamine dihydrochloride (>98%) were obtained from Thermo Scientific. Sulfanilamide was obtained from MP Biomedicals.

2.2 Characterization

Powder X-ray diffraction (XRD) patterns were recorded on a Rigaku Miniflex 600 diffractometer using Cu Kα radiation (40 kV, 15 mA) over a 2θ range of 20–60° with a step size of 0.02°. Scanning transmission electron microscopy (STEM) and transmission electron microscopy (TEM) imaging were performed using a JEOL NEOARM microscope with probe correction, operating under 200 kV accelerating voltage to examine the morphology and particle size of the Cu-CNT samples. FFT images, particle size analysis, and *d*-spacing calculations were conducted using ImageJ. X-ray photoelectron spectroscopy (XPS) was carried out on a VersaProbe 4 spectrometer to analyze the oxidation states of Cu. The metal ion concentration was quantified using inductively coupled plasma optical emission spectrometry (ICP-OES, Agilent 5800 VDV). To quantify nitrite and ammonia concentration, UV-visible spectroscopy was performed using a QE-Pro Spectrometer (Ocean Insight, Inc., USA).

2.3 Preparation of Cu-confined and Cu-attached carbon nanotube catalysts

Carbon nanotubes (CNTs) with an inner diameter of 10–20 nm and a length of 0.5–2 μm were used as catalyst supports. To remove impurities and reduce hydrophobicity, the raw CNTs were refluxed in 65% HNO_3 at 120 °C for 14 h. The acid-treated CNTs were then washed thoroughly with deionized water (18.2 MΩ cm) until a neutral pH was reached and dried at 60 °C for 12 h. Prior to impregnation, the CNTs were further vacuum-dried at 80 °C for 12 h, this material is referred to as acid-treated CNTs.

To synthesize Cu-confined CNTs catalysts (denoted Cu-in-CNT), 35 mg of acid-treated CNTs were impregnated with 1 mL of 0.8 M $Cu(NO_3)_2$ in acetonitrile. The mixture was sonicated and stirred for 30 min, followed by the dropwise addition of 0.5 mL deionized water. After an additional 30 min of sonication, the resulting material was dried at 100 °C for 10 h. To remove any Cu species attached to the external surface, the dried sample was washed with 1 M HCl, then dried again at 80 °C for 14 h. Finally, the material was calcined at 400 °C under an Ar atmosphere for 3 h to yield the Cu-in-CNT catalyst. Controlling the presence of Cu particles within CNTs was challenging due to the washing step, so their content was quantified using ICP-OES analysis post-synthesis. The maximum loading achieved for Cu-in-CNT was 2 wt%, beyond this, Cu particles attached to the CNT's exterior surface as well.

To prepare Cu-attached CNTs (denoted Cu-on-CNT), the CNTs were first refluxed at 35% HNO_3 to close the tube ends, following a previously reported method.[32,33] The end-closed CNTs were then impregnated with $Cu(NO_3)_2 \cdot 3H_2O$ solution using the incipient wetness impregnation method (water was used as the solvent instead of acetonitrile). The same drying, washing, and calcination procedure as described for Cu-in-CNT was applied to yield the Cu-on-CNT catalyst except washing with 1 M HCl.

2.4 Electrode fabrication

To prepare the working electrode, 2 mg of the Cu-CNT catalyst was dispersed in a mixed solution of deionized water (0.1 mL), ethanol (0.1 mL), and 5 wt% Nafion solution (5 μL). The resulting suspension was sonicated for 30 min to ensure uniform dispersion. Subsequently, 3 μL of the catalyst ink was

drop-cast onto a 3 mm diameter glassy carbon electrode and dried in a vacuum oven at 80 °C for 30 min.

2.5 Electrochemical studies

Electrochemical measurements were measured by potentiostat CHI 1040c in an H-type cell, which has a Nafion 117 membrane to separate the cathode and anode chambers. Graphite rod and Ag/AgCl electrode (3 M) were used as counter and reference electrodes, respectively. The working electrode was prepared by drop casting Cu nanoparticles/CNT samples with a mass loading of 0.4 mg cm^{-2}. Before each experiment, the electrolyte (phosphate buffer made from dibasic and monobasic sodium, pH 7.3) was purged with N_2 gas. The stream of N_2 gas was maintained throughout the duration of the experiment.

3 Results and discussion

To achieve selective encapsulation of Cu nanoparticles inside CNTs (Cu-in-CNT), acetonitrile was used as the solvent for dissolving the Cu precursor, taking advantage of its lower surface tension to facilitate capillary infiltration into the nanotube. To open the CNTs tube ends for encapsulation, the CNTs were pretreated by refluxing concentrated HNO_3 (65%). In contrast, to favor Cu attachment to the outer surface of CNTs (Cu-on-CNT), water was used as the solvent, and diluted HNO_3 (35%) was used for acid treatment. More experimental details are described in the Materials and experimental methods section.

A schematic illustration of Cu-in-CNT and Cu-on-CNT is shown in Fig. 1a. TEM provides direct structural evidence supporting the selective positioning of Cu nanoparticles in/on CNTs, thereby confirming the successful synthesis of the two distinct samples. The TEM image for the Cu-in-CNT in Fig. 1b clearly shows that Cu nanoparticles are placed inside the hollow cores of the CNTs. These confined particles exhibit an average particle size of ~8.7 nm, indicating controlled nucleation and growth. The TEM image for the Cu-on-CNT reveals that Cu nanoparticles of comparable size (~9.5 nm) are distributed on the outer surface of the CNTs. The particle size distributions for both samples are shown in Fig. S1. The slight difference in particle size between the encapsulated and surface-attached Cu nanoparticles suggests that spatial confinement within the CNTs limits particle growth. The Cu loadings were quantified by ICP-OES to be 2.0 wt% for Cu-in-CNT and 12.7 wt% for Cu-on-CNT.

Cu/CNT with varying Cu loadings were also synthesized, and annular dark-field scanning transmission electron microscopy (ADF-STEM) images were acquired (Fig. S2 and S3). In ADF-STEM, heavier elements such as Cu exhibit brighter contrast, enabling clear visualization of Cu nanoparticles inside the hollow channels of CNTs. These images reveal that at Cu loadings up to 2 wt%, the nanoparticles are effectively encapsulated within the CNTs, with no detectable Cu on the outer surfaces. At 3.5 wt% loading, Cu nanoparticles start to show up at the exterior of the CNTs in addition to the interior, confirming controlled encapsulation at lower loadings. Further structural analysis was conducted on the HR-TEM image of Cu-in-CNT (shown in Fig. S4), which shows the crystalline nature of the Cu nanoparticles. The symmetry and spacing of the spots in the Fourier-transformed image correspond to metallic Cu. The lattice fringes observed in the HRTEM image exhibit a *d*-spacing of approximately 0.21 nm, which is indexed to the (111) plane of metallic Cu. In contrast, the Cu-on-CNT sample exhibits a less symmetric FFT pattern, along with lattice fringes showing an interplanar spacing of approximately 0.21 nm and 0.25 nm, which can be attributed to the (111) planes of metallic Cu and CuO, respectively.

To further characterize the structure of the catalysts, Cu-in-CNT and Cu-on-CNT samples were analyzed using XRD. As shown in Fig. 1c, a prominent peak at ~26° is observed in both cases, corresponding to the (002) of graphitic carbon, confirming the presence and structural integrity of the CNT framework. For the Cu-on-CNT sample, well-defined diffraction peaks at 43.3° and 50.4° are observed, which are assigned to the (111) and (200) planes of metallic Cu, respectively. Additional peaks at 35.4° and 38.6° correspond to the (002) and (111) planes of CuO, indicating partial oxidation of the Cu nanoparticles. The presence of CuO is likely due to surface oxidation upon exposure to air during handling or storage. The XRD pattern of the Cu-in-CNT sample also shows peaks for the (111) and (200) planes of metallic Cu. However, these peaks exhibit slight shifts in position, which is likely due to lattice strain experienced by the Cu nanoparticles confined within the CNTs channels. In contrast, no CuO peaks are detected in the Cu-in-CNT sample, strongly suggesting that encapsulation within the CNTs provides a protective environment that inhibits the oxidation of Cu nanoparticles.

XPS analysis was also performed on both Cu-in-CNT and Cu-on-CNT catalysts to examine their initial oxidation states. For as-synthesized Cu-in-CNT, two prominent peaks at 952.2 and 932.4 eV were observed, corresponding to Cu $2p_{1/2}$ and Cu $2p_{3/2}$ spin–orbit couplings, respectively. The absence of satellite peaks confirmed that Cu-in-CNT primarily contained Cu(I) and/or Cu(0), with no detectable Cu(II) (Fig. 1d). In contrast, the as-synthesized Cu-on-CNT sample exhibited Cu $2p_{1/2}$ and Cu $2p_{3/2}$ at 952.4 and 942 eV, respectively, along with distinct satellite peaks around 962.2 and 942 eV, indicating the presence of Cu(II) (Fig. 1d). To further differentiate between Cu(I) and Cu(0), since their Cu 2p binding energies overlap, Auger LMM spectra were recorded. The Auger kinetic energy analysis (Cu(0) at 918.6 eV, Cu(I) at 916.7 eV, Cu(II) at 917.8 eV) revealed that the Cu-in-CNT catalyst predominantly contained metallic Cu(0), while Cu-on-CNT displayed a broad feature spanning the Cu(II) to Cu(0) region (Fig. S5).

To investigate the redox behavior of Cu in different environments, cyclic voltammetry (CV) was performed. As shown in Fig. 2a, a pair of redox peaks with a half-wave potential near −0.2 V (*vs.* Ag/AgCl) was observed, corresponding to the redox of Cu. The Cu-on-CNT sample showed sharper, better-defined peaks with smaller peak-to-peak separation (0.14 V), indicating more reversible electrode kinetics. In contrast, Cu-in-CNT exhibited broader peaks with a larger separation (0.21 V), suggesting a more sluggish redox process, likely due to the limited accessibility of the confined Cu sites. The

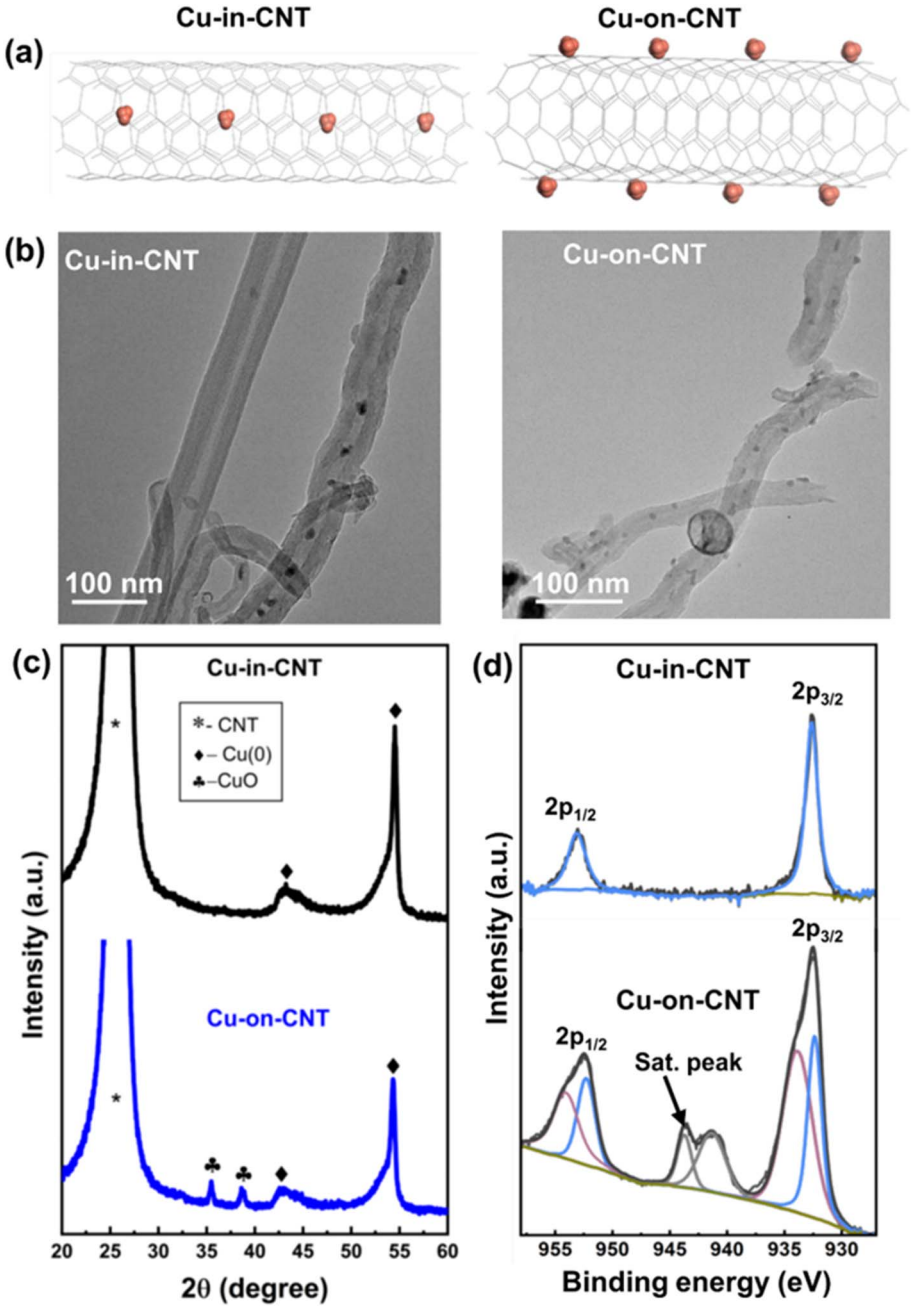

Fig. 1 (a) Schematic illustration of Cu-in-CNT and Cu-on-CNT. (b) TEM images of Cu-in-CNT and Cu-on-CNT. (c) XRD of Cu-in-CNT and Cu-on-CNT. (d) X-ray photoelectron spectra of Cu-in-CNT and Cu-on-CNT. Deconvoluted peaks correspond to Cu(I)/Cu(0) (blue), Cu(II) (red) and baseline (green).

voltammograms of CNTs without Cu were also recorded, revealing redox peaks centered around −0.12 V superimposed on a capacitive background (Fig. S6). These peaks were attributed to the redox-active functional groups in the CNTs. Baseline correction using these voltammograms enabled accurate determination of the charge associated with Cu (Fig. S7 and S8).

Fig. 2b shows the linear sweep voltammograms of Cu modified CNTs in 0.1 M phosphate buffer, normalized to the mass of electrochemically accessible Cu. In the absence of nitrate, both Cu-in-CNT and Cu-on-CNT showed negligible electrocatalytic activity; however, Cu-in-CNT displayed slightly higher non-faradaic current due to mass normalization. For both catalysts, current began to increase around −1.05 V, attributed to the onset of the hydrogen evolution reaction (HER). Upon addition of KNO_3, a significant enhancement in current was observed for both catalysts, with an earlier onset of reduction. Nevertheless, Cu-in-CNT consistently delivered higher current densities across the entire potential range, indicating superior catalytic activity, potentially due to enhanced nitrate-Cu interactions within the confined

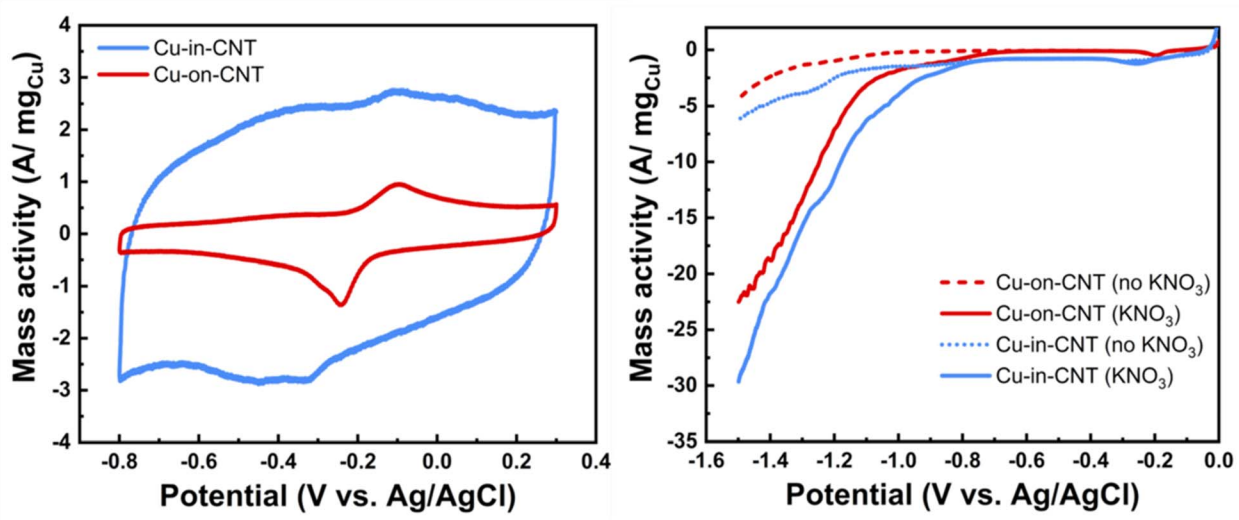

Fig. 2 (a) Cyclic voltammograms of Cu-on-CNT (2 wt%) and Cu-in-CNT (12 wt%) recorded in 0.1 M phosphate buffer (pH 7.3) at a scan rate of 30 mV s^{-1}. (b) Voltammogram of Cu-on-CNT and Cu-in-CNT in the presence and absence of 0.1 M KNO_3, recorded in 0.1 M phosphate buffer (pH 7.3). Scan rate: 10 mV s^{-1}. The current is normalized to the mass of Cu obtained from redox peaks of Cu.

environment. Notably, for Cu-in-CNT, nitrate can diffuse into the nanochannels from the opening ends of CNT and access the encapsulated Cu. Although the voltammogram of CNTs alone (65% HNO_3 treated) confirmed some catalytic activity toward nitrate reduction from CNT, Cu-in-CNT and Cu-on-CNT far outperformed bare CNTs under identical loadings (Fig. S9). Specifically, Cu-in-CNT decreased the overpotential for nitrate reduction by approximately 300 mV (from −1.1 V to −0.8 V) and achieved a current density ∼10× higher than bare CNTs at −1.5 V, underscoring the important catalytic role of Cu nanoparticles.

To evaluate the products of electrochemical nitrate reduction using Cu-in-CNT and Cu-on-CNT, chronoamperometry was performed at various potentials for 2 hours. Following electrolysis, the electrolyte was collected and analyzed to quantify the major water-soluble products, ammonia and nitrite, using the indophenol method and the Griess assay, respectively. Detailed procedures regarding product quantification are provided in the SI Section S1. Calibration curves and corresponding UV-visible spectra for the ammonia and nitrite are shown in Fig. S10. For Cu-in-CNT (Fig. 3a), the faradaic efficiency showed a clear dependence on the applied potential. At a less negative potential, nitrite was the dominant product, indicating its role as an intermediate in the reduction pathway. As the potential became more negative, nitrite formation decreased while ammonia formation increased, reaching a maximum faradaic efficiency of approximately 70 ± 6% at −1.2 V *vs.* Ag/AgCl. Beyond this potential, ammonia formation remained relatively constant, while nitrite continued to decrease, suggesting the onset of competing hydrogen evolution without further improvement in ammonia formation. For Cu-on-CNT (Fig. 3b), nitrite remains the dominant product at potentials more positive than −1.2 V. However, at −1.3 V and more negative potentials, ammonia formation increased significantly, peaking at around 65 ± 6%. At even more negative potentials, the production of nitrogen-containing products is overtaken by HER. The slightly lower ammonia selectivity for Cu-on-CNT (65% *vs.* 70% for Cu-in-CNT) suggests that the confinement in Cu-in-CNT may offer a slight advantage in ammonia selectivity. As a control, 65% HNO_3-treated CNTs was subjected to chronoamperometry at various potentials for the nitrate reduction reaction (Fig. S11). For bare CNTs, nitrite is the predominant product in the potential range of −1.2 to −1.4 V (∼50%). In contrast, the presence of Cu nanoparticles shifts the selectivity towards ammonia, making it the main product within this potential window (−1.2 to −1.5 V). These observations suggest that Cu might be the active sites that allow further reduction of the intermediate nitrite, which is accessible *via* the opening at the CNT tips. A maximum faradaic efficiency of ∼56% toward ammonia was observed at −1.5 V for bare CNTs, confirming the significant role of Cu in enhancing the nitrate reduction kinetics at less negative potentials (∼70% at −1.2 V).

After confirming the product distribution across various potentials, we investigated the effect of Cu loading on selectivity first for Cu-in-CNT. A maximum Cu loading of 2 wt% was achieved, as higher loadings (*e.g.*, 3.5 wt%) resulted in additional Cu attachment to the exterior CNTs as verified by ADF-STEM (Fig. S2). As shown in Fig. S12a, both ammonia selectivity and overall nitrate conversion efficiency increase with Cu loading, reaching ∼70% and ∼100%, respectively, at 2 wt% Cu. At 3.5 wt% loading (which contains additional Cu outside CNT), although the overall nitrate reduction was 100%, the selectivity for ammonia is lower, which is likely due to the contribution of exterior Cu nanoparticles. We also attempted to study the effect of Cu loading for Cu-on-CNT, and the results are summarized in Fig. S12b.

We subsequently evaluated the stability of the catalysts for electrochemical nitrate reduction. Chronoamperometry was conducted at the most optimized potential for each catalyst over

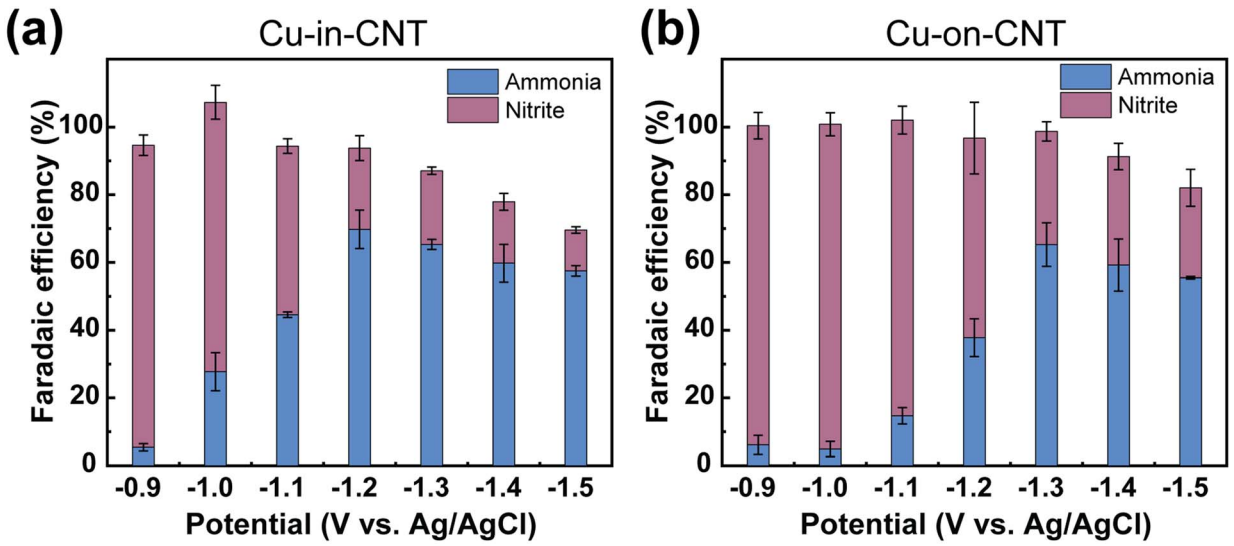

Fig. 3 Faradaic efficiency of ammonia (blue) and nitrite (red) during nitrate reduction on (a) Cu-in-CNT (2 wt%) and (b) Cu-on-CNT (12 wt%) at different potentials in phosphate buffer (pH 7.3) containing 0.1 M KNO_3. Error bars represent standard deviations from $n = 3$ samples.

12 hours. As shown in Fig. 4a, Cu-in-CNT maintains a high total Faradaic efficiency, close to 100% at 2 h, and gradually decreases to ~80% after 12 h. Notably, ammonia selectivity decreases from ~70% to ~30%, while nitrite increases from ~30% to ~50%, indicating a shift in product distribution (from ammonia to nitrite) while sustaining the overall selectivity of ~80%. Cu-on-CNT (Fig. 4b) shows a significant performance drop, with the total Faradaic efficiency decreasing from ~100% at 2 h to ~40% at 12 h. Both ammonia and nitrite production decline considerably, with ammonia dropping from ~65% to ~15% and nitrite from ~35% to ~25%. ICP-OES analysis was also performed, which revealed that Cu-on-CNT experienced substantial leaching, with 20.5 wt% of its Cu content lost to the solution, whereas Cu-in-CNT showed only 5.3 wt% Cu loss. This analysis supports our hypothesis that confining Cu nanoparticles inside CNTs significantly enhances their electrochemical stability compared to Cu-on-CNT.

The structure and phase stability of the catalysts after electrochemical nitrate reduction were evaluated using TEM and XRD, respectively. Fig. 5 shows the TEM image of Cu-in-CNT, revealing that the Cu nanoparticles largely retained their encapsulated structure within the CNTs, with an average size of ~8.0 nm (see also Fig. S13a). This observation confirms that the confinement of Cu nanoparticles within CNTs effectively prevents their agglomeration or loss during the reaction. However, some particles still migrated within the CNTs. In contrast, the TEM image of Cu-on-CNT shows particles with a broader size distribution, with particles as large as ~15–20 nm, and others that have broken down to ~3 nm (Fig. S13b). To further investigate phase changes, XRD analysis was performed on both catalysts after the reaction. For Cu-in-CNT

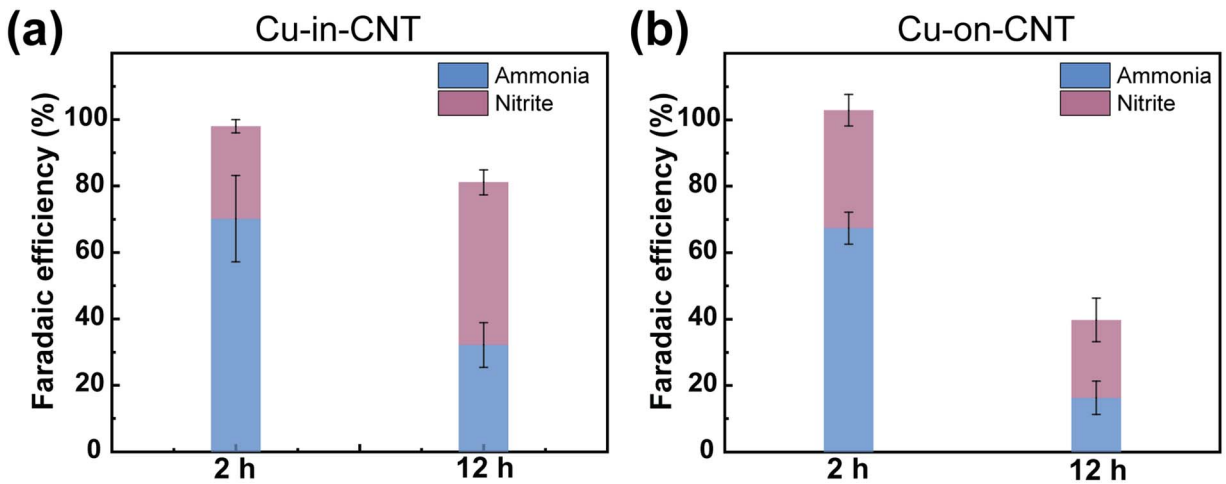

Fig. 4 Stability study of (a) Cu-in-CNT (2 wt%) (at −1.2 V) and (b) Cu-on-CNT (12 wt%) (−1.3 V) towards nitrate reduction at 2 h and 12 h in phosphate buffer (pH 7.3) containing 0.1 M KNO_3. Error bars represent standard deviations from $n = 3$ samples.

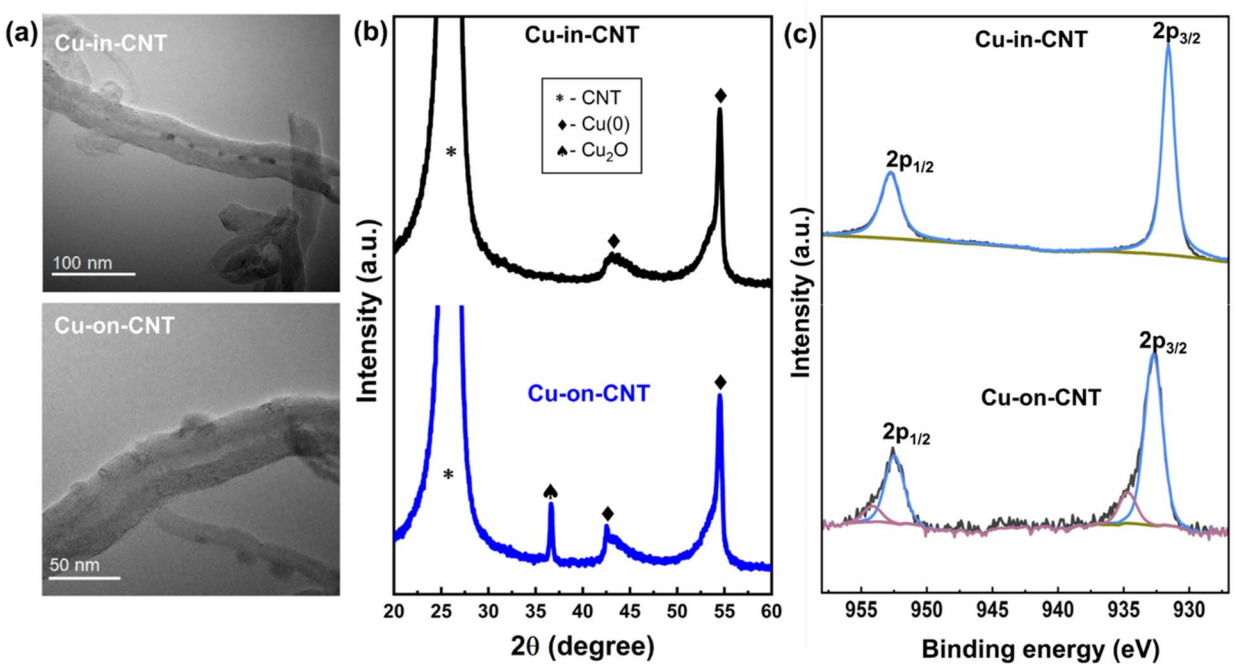

Fig. 5 Post-electrolysis characterization of catalysts. (a) TEM images of Cu-in-CNT and Cu-on-CNT. (b) XRD of Cu-in-CNT and Cu-on-CNT. (c) XPS of Cu-in-CNT and Cu-on-CNT. Deconvolution peaks correspond to Cu(II) (red line), Cu(I)/Cu(0) (blue line) and baseline (green).

(Fig. 5b), the XRD pattern confirmed the presence of metallic Cu, indicating no noticeable phase transformation. In contrast, the XRD pattern of Cu on CNTs revealed a complete disappearance of CuO peaks and the appearance of Cu_2O peaks, while metallic Cu remained detectable. This shift in phase signifies a notable change in the oxidation state of Cu during the reaction. From these studies, we support that Cu-in-CNT maintains its structural and phase integrity due to the protective role of CNTs confinement.

The post-electrolysis XPS shows that the Cu in Cu-in-CNT maintained its oxidation state, confirming the stability of the metallic Cu species (Fig. 5c). In contrast, Cu-on-CNT exhibited a significant decrease in the Cu(II) component, accompanied by an increase in Cu(I)/Cu(0) signals, suggesting partial reduction of Cu(II) during the reaction (Fig. 5c). Auger spectra further confirmed this transformation: while Cu-in-CNT remained dominated by metallic Cu(0), Cu-on-CNT displayed a pronounced metallic Cu(0) feature alongside residual Cu(II) (Fig. S14). These findings collectively indicate that Cu-in-CNT maintains its metallic state throughout the process, whereas Cu-on-CNT undergoes reduction from Cu(II) to Cu(0).

4 Conclusions

In conclusion, we have demonstrated that nanoconfinement of Cu nanoparticle catalysts significantly increases their stability and modulates their selectivity in electrochemical nitrate reduction. Specifically, by encapsulating Cu nanoparticles inside CNTs (Cu-in-CNT), the catalyst show significantly improved structural stability over 12 h compared to Cu nanoparticles supported on the exterior of CNTs (Cu-on-CNT). It was shown that Cu-in-CNT retained its metallic state before and after the electrolysis, while Cu-on-CNT underwent redox transformation. Also, a substantially lower Cu dissolution was observed during catalysis for Cu-in-CNT (5.3 wt% loss) compared to Cu-on-CNT (20.5 wt% loss). This enhanced structural robustness also translates to improved stability in product selectivity. We envision that encapsulation of catalysts inside CNTs represents a general strategy for stabilizing electrocatalysts, especially transition metals prone to redox degradation, thereby improving the overall durability of the electrocatalytic performance.

Author contributions

Tamilselvi Gurusamy: conceptualization, methodology, investigation, data curation, writing – original draft. Thomas D. Pope: methodology, investigation, review & editing. Samuel F. Wenzel: investigation, data curation, review & editing. He Zhang: investigation, review & editing. Heekwon Lee: investigation, review & editing. Hang Ren: review & editing, supervision, resources, funding acquisition, conceptualization.

Conflicts of interest

There are no conflicts to declare.

Data availability

Data supporting this article have been included as part of the supplementary information (SI). Other relevant data can be provided by the authors upon reasonable request.

Supplementary information is available. See DOI: https://doi.org/10.1039/d5ta05291b.

Acknowledgements

We acknowledge support from the Welch Foundation (F-2158-2023040) and the Sloan Foundation (FG-2023-20317). We are grateful to Dr Xun Zhan and Dr Jamie Warner for the support in TEM analysis and Dr Hugo Celio for the support in XPS study.

References

1 J. G. Chen, R. M. Crooks, L. C. Seefeldt, K. L. Bren, R. M. Bullock, M. Y. Darensbourg, P. L. Holland, B. Hoffman, M. J. Janik, A. K. Jones, M. G. Kanatzidis, P. King, K. M. Lancaster, S. V. Lymar, P. Pfromm, W. F. Schneider and R. R. Schrock, *Science*, 2018, **360**, eaar6611.
2 S. Chatterjee, R. K. Parsapur and K.-W. Huang, *ACS Energy Lett.*, 2021, **6**, 4390–4394.
3 J. W. Erisman, M. A. Sutton, J. Galloway, Z. Klimont and W. Winiwarter, *Nat. Geosci.*, 2008, **1**, 636–639.
4 V. Kyriakou, I. Garagounis, A. Vourros, E. Vasileiou and M. Stoukides, *Joule*, 2020, **4**, 142–158.
5 A. Magnino, P. Marocco, M. Santarelli and M. Gandiglio, *Adv. Appl. Energy*, 2025, **17**, 100204.
6 A. U. Shetty and R. Sankannavar, *J. Energy Chem.*, 2024, **92**, 681–697.
7 G. Qing, R. Ghazfar, S. T. Jackowski, F. Habibzadeh, M. M. Ashtiani, C.-P. Chen, M. R. Smith and T. W. Hamann, *Chem. Rev.*, 2020, **120**, 5437–5516.
8 U. B. Shahid, Y. Chen, S. Gu, W. Li and M. Shao, *Trends Chem.*, 2022, **4**, 142–156.
9 Z. Zhang, N. Zhang, J. Zhang, B. Deng, Z. Cao, Z. Wang, G. Wei, Q. Zhang, R. Jia, P. Xiang and S. Xia, *Chem. Eng. J.*, 2024, **483**, 148952.
10 S. Niu, J. Yang, L. Qian, D. Zhou, P. Du, N. Si, X. Gu, D. Jiang and Y. Feng, *ChemElectroChem*, 2023, **10**, e202300419.
11 H. Zhang, H. Wang, X. Cao, M. Chen, Y. Liu, Y. Zhou, M. Huang, L. Xia, Y. Wang, T. Li, D. Zheng, Y. Luo, S. Sun, X. Zhao and X. Sun, *Adv. Mater.*, 2024, **36**, 2312746.
12 Y. Xiong, Y. Wang, J. Zhou, F. Liu, F. Hao and Z. Fan, *Adv. Mater.*, 2024, **36**, 2304021.
13 Z. Jiang, Y. Wang, Z. Lin, Y. Yuan, X. Zhang, Y. Tang, H. Wang, H. Li, C. Jin and Y. Liang, *Energy Environ. Sci.*, 2023, **16**, 2239–2246.
14 M. Karamad, T. J. Goncalves, S. Jimenez-Villegas, I. D. Gates and S. Siahrostami, *Faraday Discuss.*, 2023, **243**, 502–519.
15 T. Hu, M. Wang, L. Ren, C. M. Li and C. Guo, *J. Phys. Chem. Lett.*, 2024, **15**, 3258–3266.
16 K. Zhang, Y. Liu, Z. Pan, Q. Xia, X. Huo, O. C. Esan, X. Zhang and L. An, *EES Catal.*, 2024, **2**, 727–752.
17 Y. Wang, A. Xu, Z. Wang, L. Huang, J. Li, F. Li, J. Wicks, M. Luo, D.-H. Nam, C.-S. Tan, Y. Ding, J. Wu, Y. Lum, C.-T. Dinh, D. Sinton, G. Zheng and E. H. Sargent, *J. Am. Chem. Soc.*, 2020, **142**, 5702–5708.
18 S. Zhang, J. Wu, M. Zheng, X. Jin, Z. Shen, Z. Li, Y. Wang, Q. Wang, X. Wang, H. Wei, J. Zhang, P. Wang, S. Zhang, L. Yu, L. Dong, Q. Zhu, H. Zhang and J. Lu, *Nat. Commun.*, 2023, **14**, 3634.
19 J. Kong, M.-S. Kim, R. Akbar, H. Y. Park, J. H. Jang, H. Kim, K. Hur and H. S. Park, *ACS Appl. Mater. Interfaces*, 2021, **13**, 24593–24603.
20 R. Ye, S. Xiao, Q. Lai, D. Wang, Y. Huang, G. Feng, R. Zhang and T. Wang, *Catalysts*, 2022, **12**, 747.
21 L. Liu, T. Chen and Z. Chen, *Adv. Sci.*, 2024, **11**, 2308046.
22 R.-P. Ye, L. Lin, Q. Li, Z. Zhou, T. Wang, C. K. Russell, H. Adidharma, Z. Xu, Y.-G. Yao and M. Fan, *Catal. Sci. Technol.*, 2018, **8**, 3428–3449.
23 J. Yuan, Z. Xing, Y. Tang and C. Liu, *ACS Appl. Mater. Interfaces*, 2021, **13**, 52469–52478.
24 V. Okatenko, A. Loiudice, M. A. Newton, D. C. Stoian, A. Blokhina, A. N. Chen, K. Rossi and R. Buonsanti, *J. Am. Chem. Soc.*, 2023, **145**, 5370–5383.
25 S. H. Lee, J. E. Avilés Acosta, D. Lee, D. M. Larson, H. Li, J. Chen, J. Lee, E. Erdem, D. U. Lee, S. J. Blair, A. Gallo, H. Zheng, A. C. Nielander, C. J. Tassone, T. F. Jaramillo and W. S. Drisdell, *J. Am. Chem. Soc.*, 2025, **147**, 6536–6548.
26 X. Bai, X. Zhao, Y. Zhang, C. Ling, Y. Zhou, J. Wang and Y. Liu, *J. Am. Chem. Soc.*, 2022, **144**, 17140–17148.
27 H. Jung, S. Y. Lee, C. W. Lee, M. K. Cho, D. H. Won, C. Kim, H.-S. Oh, B. K. Min and Y. J. Hwang, *J. Am. Chem. Soc.*, 2019, **141**, 4624–4633.
28 J. Huang, N. Hörmann, E. Oveisi, A. Loiudice, G. L. De Gregorio, O. Andreussi, N. Marzari and R. Buonsanti, *Nat. Commun.*, 2018, **9**, 3117.
29 S. Liu, Y. Li, D. Wang, S. Xi, H. Xu, Y. Wang, X. Li, W. Zang, W. Liu, M. Su, K. Yan, A. C. Nielander, A. B. Wong, J. Lu, T. F. Jaramillo, L. Wang, P. Canepa and Q. He, *Nat. Commun.*, 2024, **15**, 5080.
30 Y. Hori, H. Konishi, T. Futamura, A. Murata, O. Koga, H. Sakurai and K. Oguma, *Electrochim. Acta*, 2005, **50**, 5354–5369.
31 R. Serra-Maia, J. B. Varley, S. E. Weitzner, H. Yu, R. Shi, J. Biener, S. A. Akhade and E. A. Stach, *iScience*, 2025, **28**, 111851.
32 X. Pan, Z. Fan, W. Chen, Y. Ding, H. Luo and X. Bao, *Nat. Mater.*, 2007, **6**, 507–511.
33 D. Wang, G. Yang, Q. Ma, M. Wu, Y. Tan, Y. Yoneyama and N. Tsubaki, *ACS Catal.*, 2012, **2**, 1958–1966.